Measurement of pion-proton bremsstrahlung for pions at 299 MeV

C. A. Meyer,[b,*] C. Amsler,[a] A. Bosshard,[a] K. M. Crowe,[b] M. Döbeli,[a] M. Doser,[a] L. van Elmbt,[a,†] R. P. Haddock,[c] Q. Ingram,[d] S. Ljungfelt,[b,‡] J. F. Loude,[e] J. P. Perroud,[e] J. Riedlberger,[a] D. Renker,[d] M. Schaad,[a,§] D. I. Sober,[f] and P. Truöl[a]

[a]*Physik-Institut der Universität Zürich, CH-8001 Zürich, Switzerland*

[b]*University of California, Berkeley and the Lawrence Berkeley Laboratory, Berkeley, California 94720*

[c]*University of California—Los Angeles, Los Angeles, California 90024*

[d]*Schweizerisches Institut für Nuklearforschung, CH-5234 Villigen, Switzerland*

[e]*Institut de Physique Nucléaire, Université de Lausanne, CH-1015 Lausanne, Switzerland*

[f]*Catholic University of America, Washington, D.C. 20064*

(Received 13 October 1987)

We have measured the fivefold differential cross section $d^5\sigma/d\Omega_\pi d\Omega_\gamma dE_\gamma$ for the process $\pi^+ p \to \pi^+ p\gamma$ with incident pions of energy 299 MeV. The angular regions for the outgoing pions ($55° \le \theta^\pi_{\rm lab} \le 95°$), and photons ($\theta^\gamma_{\rm lab} = 241° \pm 10°$) in coplanar geometry are selected to maximize the sensitivity to the radiation from the magnetic dipole moment of the $\Delta^{++}(1232)$ resonance. At low photon energies, the data agree with the soft-photon approximation to pion-proton bremsstrahlung. At forward pion angles the data agree with older data and with the latest theoretical calculations for $2.3\mu_p \le \mu_\Delta \le 3.3\mu_p$. However at more backward pion angles where no data existed, the predictions fail.

I. INTRODUCTION

In radiative pion-proton scattering, $\pi p \to \pi p \gamma$, one studies the strong πp interaction with a well understood electromagnetic probe. In doing so, the range and validity of the soft-photon approximation to the bremsstrahlung cross section as well as the electromagnetic properties of intermediate resonances and the off-mass-shell πp interaction can be examined. The experimental history of this type of measurement is almost entirely restricted to a 1975 experiment performed at the Berkeley 184-in. cyclotron by the UCLA group.[1-3] The UCLA experiment has looked at both π^+ and π^- scattering at several incident pion energies and photon angles, but in many cases with limited statistics due to the low intensity of the pion beam. There are also data on the $\pi^- p$ system from the OMICRON experiment[4] at the CERN Synchrocyclotron (SC). The small amount of data available has presented a considerable challenge to theoretical interpretations with a majority of the models failing to reproduce the features of the data.

In the most straightforward model, the soft-photon approximation (SPA), one expresses the bremsstrahlung cross section as an expansion in powers of the photon energy k. In the soft-photon limit, Low[5] has shown that the amplitude M_γ for a radiative process is expressed as a power series in photon energy:

$$M_\gamma = \frac{m_0}{k} + m_1 + m_2 k + \cdots ,$$

where the first two terms m_0 and m_1 are calculated exactly from the elastic amplitude and its derivatives with respect to energy. These two terms are the usual soft-photon calculation and the graphs contributing to $\pi p \to \pi p \gamma$ are shown in Figs. 1(a)–1(d). In the standard SPA calculation, one considers only the external bremsstrahlung, but in trying to extend this model to higher orders, internal bremsstrahlung needs to be included [Fig. 1(e)]. Comparisons of simple SPA calculations to the UCLA data[1] show that these calculations are valid for photon energies below 35 or 40 MeV. Another SPA-type model is external-emission dominance[6] (EED). In EED only the first term in the SPA expansion of M_γ is used which gives a $1/k$ falloff with photon energy. This agrees well with the UCLA data out to the highest measured photon energies; however, there is no good understanding of the dynamical reasons for this result. The most recent, refined SPA calculations, by Liou and Nutt[7] fit the UCLA data quite well out to photon energies of 100 MeV.

Since the NN interaction is modeled in terms of meson exchange where the meson is typically off mass shell, a better understanding of the off-mass-shell πp interaction could lead to a better understanding of the NN interaction. In principle, pion-proton bremsstrahlung can be used to probe the off-mass-shell πp interaction. However, the success of the SPA models indicate that the coupling of the photon to the strongly interacting system is too weak to significantly influence the πp interaction. In the geometries of $\pi p \to \pi p \gamma$ experiments performed so far, the photon is detected in a backward direction relative to the scattered pion and proton. This geometry leads to constructive interference between the external pion and proton radiation for negative pions and destructive interference for positive pions. As it is radiation from the external particles which leads to off-mass-shell effects, the $\pi^- p$ system is better suited to this study than $\pi^+ p$. Furthermore, the radiation from the intermediate Δ^0 in the $\pi^- p$ system is minimal [the Δ^0 has zero charge and,

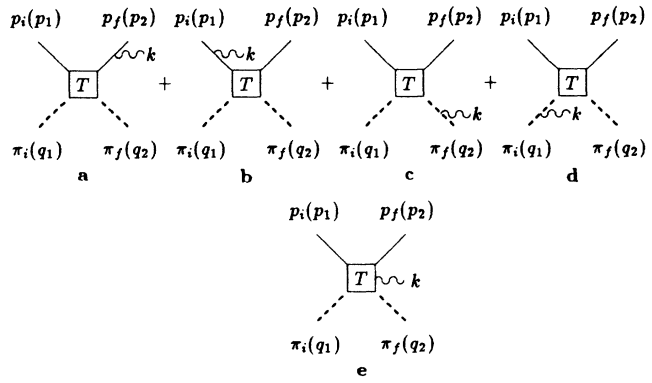

FIG. 1. Diagrams included in an SPA (soft-photon-approximation) calculation for $\pi p \to \pi p \gamma$: (a–d) external bremsstrahlung, (e) internal bremsstrahlung (not considered in normal SPA calculation). $T(s,t)$ is the πp scattering amplitude evaluated at (s,t).

according to SU(3), zero magnetic dipole moment]. Of course the off-mass-shell effects are still present in the $\pi^+ p$ system, although mixed with radiation from the intermediate Δ^{++} and minimized by the destructive interference.

Finally, it is possible to probe the electromagnetic properties of the intermediate Δ by studying the process $\pi p \to \Delta \to \Delta\gamma \to \pi p \gamma$, where the Δ decays to itself due to its large width, proceeding primarily through a magnetic dipole interaction. For $\pi^+ p$, one has both destructive interference of the external radiation and the maximum internal contribution (Δ^{++}). It is primarily this feature which has motivated the πp bremsstrahlung program.

In order to obtain information about the electromagnetic properties of the intermediate Δ, one has to be able to relate a measured cross section $d^5\sigma/d\Omega_\pi d\Omega_p dE_\gamma$ to the various electromagnetic moments of the Δ. Fischer and Minkowski[8] have worked on this in terms of the SPA model by calculating the terms of order k in the expansion for M_γ. Alternatively, one may describe the πp interaction with an isobar model, and then add the bremsstrahlung terms according to the rules of quantum electrodynamics. We will not discuss the history of this type of calculation, but instead refer to the literature.[9–13] The most recent isobar calculation is from MIT (Refs. 14–17), and details of this model will be discussed later.

Theoretical predictions for μ_Δ can be obtained from any model which predicts magnetic moments of the baryon octet. Predictions from SU(3), SU(6) (Ref. 18), and the quark model,[19] all give $\mu_\Delta = 2.0\mu_p$. Bag-model corrections to the quark model[20] predict a value 17–21 % smaller. When the MIT theory is fitted to previous data,[17] a value between 2.5 and $3.5\mu_p$ is obtained for μ_Δ.

Our primary interest in performing this experiment has been to extract information on the magnetic dipole moment of the intermediate $\Delta^{++}(1232)$. This goal is strongly motivated by the MIT theory, and in particular a prediction of the theory that a measurement of the spin asymmetry with a polarized proton target,

$$\gamma = \frac{d^5\sigma\uparrow/d\Omega_\pi d\Omega_\gamma dE_\gamma - d^5\sigma\downarrow/d\Omega_\pi d\Omega_\gamma dE_\gamma}{d^5\sigma\uparrow/d\Omega_\pi d\Omega_\gamma dE_\gamma + d^5\sigma\downarrow/d\Omega_\pi d\Omega_\gamma dE_\gamma},$$

is a very sensitive probe of μ_Δ while being particularly insensitive to the ambiguities and uncertainties of the model. The experiment is divided into two parts: (1) measurement of the unpolarized cross section $d^5\sigma/d\Omega_\pi d\Omega_p dE_\gamma$ and (2) measurement of the polarization asymmetry γ. This paper reports on the first half of the measurement of pion-proton bremsstrahlung, $\pi^+ p \to \pi^+ p \gamma$ with 299-MeV incident pions on an unpolarized hydrogen target. Pions are detected in the laboratory at angles between $\theta_\pi = 55°$ and $\theta_\pi = 95°$, while the photons are detected near $\theta_\gamma = 119°$ on the opposite side of the incident beam in a coplanar geometry. A second measurement, to be reported later, uses a polarized hydrogen target to make a measurement of the spin asymmetry γ in nearly identical geometries.

II. THE EXPERIMENTAL APPARATUS

A drawing of the experimental apparatus is shown in Fig. 2. We detect all three particles in the final state, and measure pion momentum and direction, photon energy and direction, and the proton energy and in-plane direction. Our coordinate system has its origin at the center of the target. The $+z$ axis is along the incident pion beam, $+y$ is vertical, and $+x$ points away from the magnetic spectrometer.

A. The pion beam

The experiment has been performed in the SIN IIE1 area[21] using a 421.6-MeV/c beam of positive pions. The momentum of the beam has been measured during the run by time-of-flight difference between pions and protons. The beam composition is measured to be $p/\pi^+ \approx 13/1$ and $e^+/\pi^+ < 0.01/1$. After insertion of carbon absorbers into the beam, the composition is measured to be $p/\pi^+ < 0.005/1$. The experiment has been performed with the carbon absorbers in place. The muon contamination is calculated by Monte Carlo methods to be $\mu^+/\pi^+ \approx 0.045/1$. The divergence of the beam is measured to be 7 mrad, and the beam spot at the center

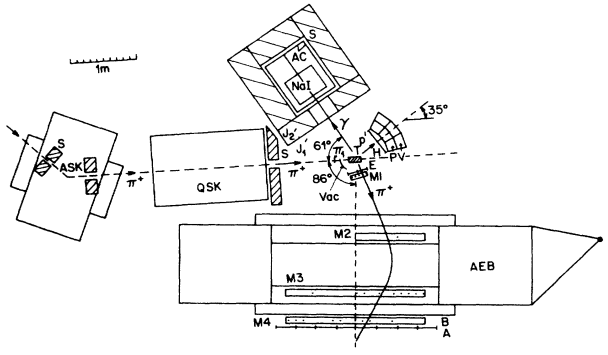

FIG. 2. Experimental setup for the experiment. AEB: pion spectrometer magnet; ASK: bending magnet; QSK: quadrupole triplet; S: lead shielding. $M1$,$M2$,$M3$,$M4$: multiwire proportional chambers, P,H,E, A,B, AC,$J1$,$J2$,V; π_1: plastic scintillators; T: liquid-hydrogen target; Vac: shows the radius of the vacuum jacket around the target; NaI: sodium iodide array. The π^+'s are the incident and scattered pions, p' is the final-state proton, and γ is the detected photon.

of the target is 13 mm [full width at half maximum (FWHM)] wide and 19 mm (FWHM) high. The incident flux has been monitored by a telescope of two scintillators $J1$ and $J2$ which looks at the upstream side of the target's outer vacuum jacket. These counters are calibrated against an in-beam counter (π_1 in Fig. 2) at 0.50, 1.0, and 2.0 MHz. $J1$ and $J2$ are then used to measure the 26-MHz flux used in the experiment. The beam momentum at the center of the target is 415.8 MeV/c with a momentum byte ($\Delta p/p$) of 0.6% (FWHM).

B. The detector

The main component of the pion spectrometer is a large picture-frame magnet of active volume $1250\times650\times520$ mm^3. The central field is 0.68 T, and the pions are tracked with four multiwire proportional chambers ($M1$,$M2$,$M3$,$M4$) and three arrays of plastic scintillators (E,B, A).

The E array identifies pions entering the spectrometer and consists of two counters $150\times200\times3$ mm^3 located in front of $M1$. The B and A arrays define the pion's exit. Both of these arrays consist of eight counters $300\times500\times3$ mm^3 which sit behind $M4$. Pulse-height and timing information from E and B is recorded for each event. The time of flight between the E and B arrays gives a sharp peak of width 3.1 ns (FWHM) for pions, while protons appear in a 100-ns-long tail. A combination of pulse-height and time-of-flight information suffices to distinguish between pions and protons and has been used at the lowest level of the analysis.

$M1$ (144×144 mm^2) and $M2$ (1000×480 mm^2) track pions entering the magnet, while $M3$ and $M4$ (2120×480 mm^2) track exiting pions. $M1$ has sense planes at 90°, 0°, 45°, and 135°, while $M2$, $M3$, and $M4$ have planes at 60°, 90°, and −60°. All wire spacings are 2 mm, and each sense wire is individually read out. A more detailed mechanical description of the chambers, and of the readout electronics can be found elsewhere.[22] The magnetic field is monitored by a Hall probe mounted in the magnet. The Hall probe has been calibrated against a proton NMR signal.

The proton detector consists of three parts: a ΔE hodoscope of 12 counters, H, an array of 3 thick plastic blocks P, and an array of 3 veto counters, V. A proton is defined as $H_j\cdot P_i\cdot\bar{V}_i$, where the H_j is in front of the P_i. There is also pile-up logic to tag those events with more than one particle arriving per 150 ns in any P counter.

The hodoscope array H consists of strips of NE102A plastic scintillator ($34\times480\times5$ mm^3) with a Hamamatsu R1450 photomultiplier tube on each end. The time-of-flight resolution is insufficient for particle discrimination due to the short flight path.

The large plastic blocks P and V are 150 mm thick and read out at one end with a Philips XP-2041 photomultiplier tube. The P will stop up to 150 MeV protons and their performance is described elsewhere.[23,24] A light-emitting-diode (LED) flash system connected to the plastic blocks is used to monitor the gains of the detector. The stability of the flash system is checked by looking at the pulse height of elastic protons in the large plastic blocks during each run. The elastic protons from πp scattering are selected by requiring a pion within a narrow momentum and angular window to be present. The gain constants vary by less than 8% from the calibration run, and run by run corrections are applied. Calibration of the system is accomplished by examining protons from elastic πp scattering in conjunction with reconstructed pions.

The resolution of the proton detector is measured by examing elastic events. We obtain an angular resolution of 3.8° (FWHM) which is in agreement with the angular width of a hodoscope strip of 4.75°. The energy resolution of the proton detector is measured to be 5.2 MeV (FWHM) at 100 MeV. An additional uncertainty of 6.0 MeV (FWHM) stems from an uncertainty in the interaction point within the target.

The photon detector is a square array of 64 NaI(Tl) crystals ($63.5\times63.5\times400$ mm^3, 15.4 radiation lengths deep) and has been described previously.[25] The crystal array is surrounded by plastic scintillator counters on the top, bottom, left, and right for vetoing cosmic events and a 1-cm-thick plastic scintillator in front to veto charged particles. The shielding of the NaI crystals, except for the entrance window, is made up of 5 cm of lead, 20 cm of borated polyethylene, 1.5 mm of cadmium, and another 10 cm of lead. Each crystal is looked at with a Philips 2202 photomultiplier tube which is optically coupled to a flash system via an optical fiber. The array is positioned at $\theta_\gamma=119°$ and sits 107 cm from the center of the target.

The photon trigger requires a minimum energy deposited in the NaI(Tl) array. This is done by forming all possible sums over 2-by-2 subarrays of crystals, and requiring at least one sum to be above a minimum threshold. This hardware threshold is set at 13 MeV, but because of slight differences between individual crystals an off-line cut of 15 MeV is applied. The time resolution obtained with constant fraction discriminators is 1.8 ns (FWHM). The crystals are calibrated with a ^{137}Cs source, cosmic muons, and photons from the reaction $\pi^-p\rightarrow n\gamma$ (where the π^- stop in the liquid-hydrogen target). We measure a resolution of 9.5% (FWHM) at the 129-MeV line, while the energy dependence of the detector resolution can be parametrized as

$$R\ (\%\text{FWHM})=\frac{200}{E_\gamma\ (\text{MeV})}+8$$

for photon energies above 10 MeV.

The liquid-hydrogen target is a Mylar cylinder 45 mm in diameter with domes on both ends. The overall length of the target is 140 mm, and it presents about 1 g/cm^2 to the incident pion beam. The target walls are about 75 μm thick at the entrance and exit, and average about 130 μm thick over the rest of its surface. The vessel is wrapped in superinsulation and sits inside of a vacuum vessel with approximately 500-μm-thick Mylar windows. The support member for the target is placed between the incident pion beam and the scattered pion. The hydrogen is cooled with liquid helium and a control system maintains the pressure above the target to within set limits.

The liquid-hydrogen density is determined from standard density tables.

C. The acceptance of the detector

The effective solid angle of the apparatus is calculated by Monte Carlo methods (see next section) using $\pi p\gamma$ events from a phase-space distribution (Fig. 3). The sharp cutoff in the πp acceptance at high photon energy arises from undetected forward protons. Corrections for experimental inefficiencies are applied as follows.

In the analysis, events with a photon energy below 15 MeV are discarded. Because of resolution and efficiency effects, some photons with $E_\gamma > 20$ MeV are lost in this cut. Using the known response of the detector,[25] the fraction lost as a function of energy can be calculated. This correction is 18% at 20 MeV, and negligible above 25 MeV. Shower leakage into the veto counters contributes a nearly energy-independent inefficiency of 8.7±3.0%. This is dominated by electrons (positrons) backscattered into the entrance veto counter.[25] Corrections are also made for photons which hit one of the central 6-by-6 crystals, but deposit most of their energy in an outside crystal (6% at 20 MeV and 12% at 100 MeV). Events which are not centered in one of the 6-by-6 inside crystals are rejected because of large shower leakage.

The acceptance of the proton detector is corrected for protons scattered in the target, the target vessel, the air, and the hodoscope and also for nuclear interactions in the detector itself. These corrections are energy dependent and are computed from published data.[26,27] They vary between 5.2% at 50 MeV and 19.5% at 150 MeV. For two energies these corrections have been checked experimentally by requiring only a reconstructed pion to define a πp-elastic event and recording the number of protons actually found in the expected proton counters. For two of the proton counters we measure 14.3±3.5% and 10.9±2.6%, respectively, while calculations for the same counters yield 15.2% and 9.1%. Finally, pile-up corrections [more than one proton arriving in the same analog-to-digital converter (ADC) gate], between 3% and 7% are applied.

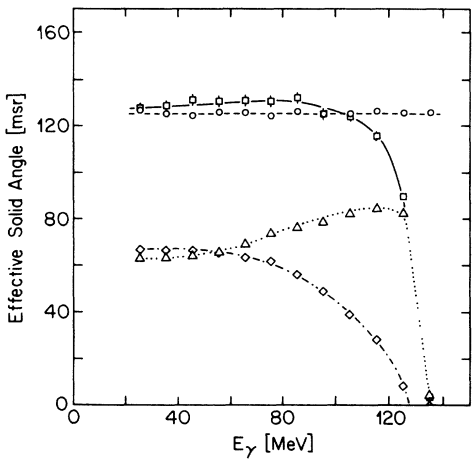

FIG. 3. Effective solid angle of the NaI array and the magnetic spectrometer. NaI array: ○, the entire magnetic spectrometer requiring that the proton be detected: □, the magnetic spectrometer for pions between 55° and 75°: △, pions between 75° and 95°: ◇.

The acceptance of the pion spectrometer has been corrected for pion decay, chamber reconstruction efficiency, multiwire proportional chamber (MWPC) efficiencies, and inefficiencies of the pion counters. The latter are determined from separate runs in which a given counter has been left out of the trigger. The combined inefficiency of all the plastic counters is measured as 2.5±1.4%. The combined efficiency of the wire chambers are measured on a run-by-run basis and varies from 30% to 55%. The low efficiency and the large variation in efficiency results from a random, but easily identified noise in $M2$ (more than 40 wires firing). This inefficiency only affects the statistics of the final data sample. A measured reconstruction efficiency of 95±2% has also been included. Pion decay and pole-tip scattering are studied by Monte Carlo simulation. The corrections vary from 15% for 220 MeV/c pions to 10% for 330 MeV/c pions.

III. DATA REDUCTION AND ANALYSIS

A. Particle reconstruction

Reconstruction of the final-state pion is done with a set of tracking functions. The arguments of the functions are linear combinations of the fired wires in an event, and the values of functions are the pion momentum, initial angles, and interaction point. To determine the tracking functions, about 4000 Monte Carlo pion tracks which fill the phase space of the spectrometer are generated. A principal-components analysis is performed on these tracks to obtain the transformation from wire space to principal-component space. The principal components η_i can be written in terms of the wires $\mathbf{w}_i$ as

$$\eta_i = \mathcal{A}(\mathbf{w}_i - \mathbf{c}) ,$$

where $\mathcal{A}$ is a rotation matrix and $\mathbf{c}$ is an offset. The Monte Carlo tracks are next used to generate a set of functions of the principal components for momentum, angles at the target, and target traceback. These functions are of the form

$$f(\eta) = \sum_\alpha P_{\alpha 1}(\eta_1) P_{\alpha 2}(\eta_2) \cdots P_{\alpha n}(\eta_n) ,$$

where the $P_{\alpha i}(\eta_j)$ are the ith Chebychev or Hermite polynomial of the jth principal component for the αth term in the function. A typical function contains 50 of the above terms with between 1 and 7 principal components in each term. A more detailed description of this method for a different arrangement of the chambers and magnet used in this experiment is given in Ref. 22. With the resulting functions, we are able to reconstruct the Monte Carlo momentum to ±4.2 (MeV/c) (FWHM), the pion θ and ϕ angles to ±0.80° (FWHM) (this includes effects due to multiple scattering in the detector), and the target traceback to ±3 mm (FWHM).

Tracking of particles in the Monte Carlo simulation is

performed using a Runge-Kutta integration procedure on the equations of motion. The magnetic field is determined from a map measured at 0.80 T and scaled down to the 0.68 T used in the experiment. The physical positions of the chambers have been surveyed at the end of each run period and chambers are aligned by software using straight tracks taken from field-off runs.

Track finding consists of locating at least one B-array element within allowed time-of-flight windows. The wire-chamber information is then examined to determine if sufficient wires fired in all four chambers to reconstruct the event. Fired wires are grouped within a given chamber such that their intersections form sufficiently small triangles. These triangles are then associated to form tracks. The reconstructed tracks are required to come from within the target volume and point toward an in-time B paddle. Finally, p_π, θ_π, and ϕ_π are reconstructed.

The resolution of the reconstructed events is measured by examining elastic πp events. We calculate the difference between the measured elastic momentum, and the elastic momentum as calculated from the scattering angle of the pion. We then unfold the angular resolution of the system, the angular distribution of incident pions, the momentum distribution of incident pions, and the uncertainty of the depth in the target from which the pion came. When these effects are removed, a pion momentum resolution of 5.3 MeV/c (FWHM) is obtained.

Reconstruction of the protons is done by first identifying all hodoscope bars which fired within allowed time-of-flight and pulse-height windows. These are then matched to fired proton counters (without pile-up or veto). If a hodoscope can be matched with two fired proton counters, it is associated with the one containing the most energy. The proton's energy is then calculated as

$$E_p = E_{\text{plastic}} + \Delta E_{\text{hodo}} + \Delta E_{\text{targ}} + \Delta E_{\text{air}} + \Delta E_{\text{wrappings}} ,$$

where E_{plastic} and ΔE_{hodo} are measured in the detector (P and H) and the other quantities are calculated based upon the protons trajectory. The energy lost in the target ΔE_{targ} is an average formed by computing the energy loss of the proton from three points along the pion's trajectory through the target. ΔE_{air} is the energy lost in the air, and $\Delta E_{\text{wrappings}}$ is the energy lost in the material wrapping the plastic scintillators.

Reconstruction of the photon begins with a search through all the fired crystals to identify the one with the most energy deposited in it. All bars with less than 0.4 MeV in them are ignored, which removes noise coming from pedestal subtractions and activation of the crystals. The bar containing the most energy must be within allowed time-of-flight windows, and not be one of the 28 bars around the outside of the array. If the above conditions are met, a search of the 5-by-5 subarray of crystals centered on the one containing the most energy is made and all bars with a nonzero ADC reading are added into the total energy. No time-of-flight cut is placed on the secondary bars because if the amount of deposited energy is small, it is unlikely that a time-to-digital converter (TDC) stop would be recorded. The time of the event is then computed by taking the energy weighted average of the times of all bars in the event which are within ± 3 ns of the maximum bar. Finally the position of the hit is calculated by forming an energy weighted sum of each crystal which fires.

The time-of-flight window in the hardware trigger has been left quite wide in order to study background contributions to the trigger. These backgrounds are discussed in the next section. In order to remove most of this background, only events in a 6.1-ns wide window about the central photon time are accepted. With the 1.8-ns FWHM time resolution of the NaI(Tl) array, this cut is at the 4σ level. About 20% of the trigger survives this cut, and good photon timing is critical in minimizing the surviving background.

B. Backgrounds

Because of the good timing and pulse-height information available in the pion and proton detectors, it is unambiguous to identify these particles. Backgrounds arise when a photon is included in the event. Figure 4 is a typical time spectrum of all photons from a $\pi^+ p \to \pi^+ p \gamma$ trigger. The photons can be divided into two sources: correlated and uncorrelated with the beam pion. The backgrounds have been divided along these lines.

The dominant source of random NaI triggers comes from muon-decay positrons. Pions which backscatter into the NaI(Tl) array will stop near the middle of the detector and decay ($\pi^+ \to \mu^+ \nu_\mu$), the muons then decay ($\mu^+ \to e^+ \nu_e \bar{\nu}_\mu$) producing positrons which are distributed uniformly in time. Another source comes from pions which charge exchange on material in the target ($\pi^+ N \to \pi^0 X$). This reaction can occur when there are more than one pion in a given beam burst, or when the charge-exchange pion comes from one of the adjacent bursts. Except at the very lowest photon energies both these triggers require an inelastic pion or proton in order to survive the analysis. One inelastic source is pions which decay in the magnet and have the wrong momentum assigned to them. Nuclear reactions can also generate inelastic events, e.g., $\pi^+ N \to \pi^+ p X$.

To study these uncorrelated backgrounds, a software cut has been made which selected events in which the NaI trigger comes from one beam burst after the pion and proton triggers. When this sample is analyzed in exactly the same manner as the in-time NaI triggers, a subtraction for all the uncorrelated backgrounds is obtained. This subtraction removes the contributions from elastic or quasielastic πp's in coincidence with muon-decay positrons and NaI triggers caused by more than one pion per beam burst.

A source of correlated NaI triggers is quasifree bremsstrahlung, which may occur in the target walls. In this reaction, the bremsstrahlung is off a bound proton, which is then knocked free. Evidence for this reaction is looked for by analyzing events which come from near the target windows. The spectrum from this region is no different from that at the center of the target. In particular if the reaction is present to any large degree one expects a small peak in the energy balance at the binding energy of carbon in the reaction $\pi^+ {}^{12}\text{C} \to \pi^+ p {}^{11}\text{B}\gamma$. No such peak is

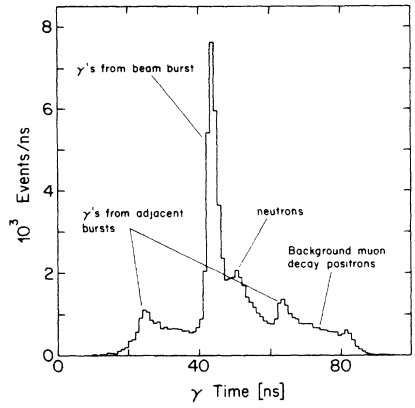

FIG. 4. Time spectrum of all detected photons during a $\pi^+p\to\pi^+p\gamma$ run.

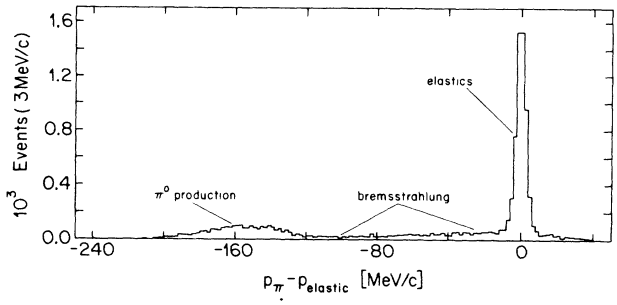

FIG. 5. Pion momentum difference $p_\pi^{meas}-p_\pi^{elas(\theta)}$ for the raw data sample. The peak labeled *elastics* contains elastic πp events in coincidence with a random NaI trigger. The peak labeled π^0 arises from the reaction $\pi^+p\to\pi^+\pi^0p$. The region labeled *bremsstrahlung* contains the events from $\pi^+p\to\pi^+p\gamma$.

visible. The reaction $\pi^+n\to\pi^0p$ can occur on bound neutrons in the target walls. If the pion then decays via $\pi^0\to\gamma e^+e^-$ and the e^+ is misidentified as a π^+, a false-bremsstrahlung signal could occur. Because of both the kinematic constraints on the final system, and the kinematics of this decay, it could only contribute for $E_\gamma<30$ MeV. In this region we calculate that its contribution is less than 1% of the $\pi^+p\to\pi^+p\gamma$ signal. Analysis of empty target data, and study of the signal coming from near the target windows show no evidence of backgrounds at a level of 4% of the signal. No target subtraction is performed. The reaction $\pi^+p\to\pi^+\pi^0p$ is also a beam-correlated background, and is discussed in the next section.

C. Event determination

The data written to tape contain a large number of events in which a proton is seen in the magnetic spectrometer, and either a pion or a beam muon is seen in the proton detector. A very small fraction of these events are actually data from the reverse $\pi^+p\to\pi^+p\gamma$ reaction (the pion seen in the proton detector, and the proton seen in the magnetic spectrometer), but most are just unwanted background. In order to remove these events, a cut on pulse height and timing in both the pion and proton detectors has been made. This cut removes about 60% of the $\pi^+p\to\pi^+p\gamma$ events written to tape. We did not try to analyze the reverse $\pi^+p\to\pi^+p\gamma$ reaction because (1) there is a very small solid angle for it, particularly at high photon energies and (2) there exists a large muon background in the proton detector at low photon energies.

The surviving events are reconstructed for $(p_\pi,\phi_\pi,\theta_\pi)$, (E_p,α_p), $(E_\gamma,\phi_\gamma,\theta_\gamma)$, and (y_{targ},z_{targ}). Requiring only that an in-time π^+, p, and γ are reconstructed, reduces the data set to 2.2% of that written to tape. The lost events in the order of cutting are made up of 60% π and p not correlated, or in the wrong detectors, 25% have insufficient recorded data to reconstruct, and 13% do not have an in-time photon. This remaining data set is referred to as the raw data set.

Most of the events in the raw data set are elastic scattering in coincidence with a random NaI trigger. By examining the pion spectrometer alone, it is possible to eliminate most of theses events. Taking p_π^{meas} as the reconstructed pion momentum, and $p_\pi^{elas(\theta)}$ as the calculated momentum of an elastic pion at an angle θ, the difference $p_\pi^{meas}-p_\pi^{elas(\theta)}$ (see Fig. 5) is small for elastic events. For $\pi^+p\to\pi^+p\gamma$ events, it can be parametrized as

$$p_\pi^{meas}-p_\pi^{elas(\theta)}\approx 0.86E_\gamma(\text{MeV}) ,$$

and by cutting at

$$p_\pi^{meas}-p_\pi^{elas(\theta)}<-9.0\ \text{MeV}/c , \tag{1}$$

we lose less than 2% of the good events in the lowest-energy range, and none above that.

In order to remove more of the elastic events, the charged-particle energy balance $E_{\pi p}$ is formed (see Fig. 6):

$$E_{\pi p}=E_{\text{in}}+m_p-E_\pi-E_p .$$

E_{in} is the energy of the incident pion, m_p is the proton mass, E_π is the detected pion's energy, and E_p is the detected proton's energy. This quantity should be zero for elastic events, and have a long positive tail for bremsstrahlung events. In order that fewer than 1% of the events in the lowest-energy bin are lost, a cut at

$$E_{\pi p}>0\ \text{MeV} \tag{2}$$

has been made.

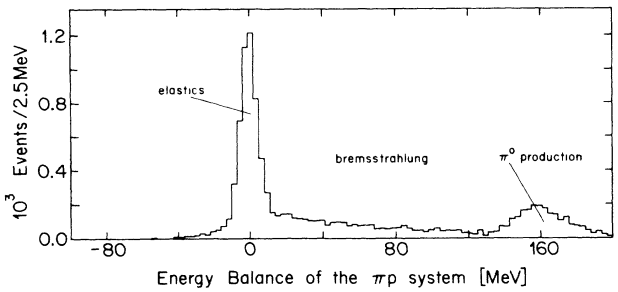

FIG. 6. Charged-particle energy balance (the reconstructed photon is ignored).

Finally, to remove elastic events in which the pion decays in the magnet, or a pion rescatters in the liquid-hydrogen target (about 1.5% of the time), a cut on the proton's deviation from elasticity has been made. If p_p^{meas} is the measured proton momentum, and $p_p^{\text{elas}(\alpha_p)}$ is the calculated elastic proton momentum at the in-plane angle α_p then

$$p_p^{\text{meas}} - p_p^{\text{elas}(\alpha_p)} \approx -2.06 E_\gamma \ ,$$

for $\pi^+ p \to \pi^+ p \gamma$ events. A cut at

$$p_p^{\text{meas}} - p_p^{\text{elas}(\alpha_p)} < +10.0 \text{ MeV}/c \tag{3}$$

removes less than 1% of all good events in the lowest-energy bin.

A background in which the photon is correlated with the pion and proton arises from the process $\pi^+ p \to \pi^+ \pi^0 p$. By defining a πp missing mass (disregarding the photon) as

$$m_X^2 = (E_{\text{in}} + m_p - E_\pi - E_p)^2 - |\, \mathbf{p}_{\text{in}} - \mathbf{p}_\pi - \mathbf{p}_p \,|^2 \ ,$$

these events can be cleanly separated from the bremsstrahlung events. E_{in}, m_p, E_π, and E_p have already been defined, $\mathbf{p}_{\text{in}}$ is the incident pion's momentum, $\mathbf{p}_\pi$ is the scattered pion's momentum, and $\mathbf{p}_p$ is the scattered proton's momentum. For elastic and bremsstrahlung events, m_X^2 is peaked at 0, whereas for $\pi^+ p \to \pi^+ \pi^0 p$ it is peaked at $m_{\pi^0}^2 = 18\,200$ MeV^2. To remove the π^0's, the cut

$$m_X^2 < 7500 \text{ MeV}^2 \ , \tag{4}$$

is made. Figure 7 shows m_X^2 for all events in the raw data set, and for all events surviving cuts 1–4.

Finally, the difference between the measured in-plane proton angle α_p^{meas} and the proton angle which best balances the $\pi p \gamma$ system is examined:

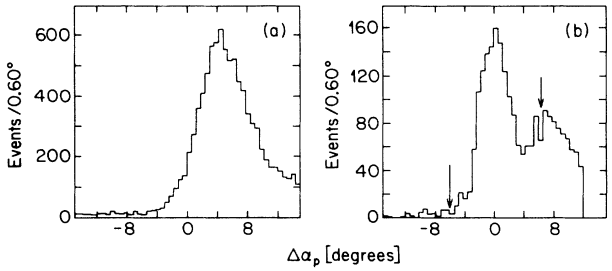

FIG. 8. Difference between the measured proton angle α_p and the angle needed to best balance the overall momentum of the system. (a) All reconstructed events. (b) After cuts 1–4. The arrows indicate cut 5.

$$\Delta\alpha_p = \alpha_p^{\text{meas}} - \arctan\left[\frac{-p_\pi^x - p_\gamma^x}{p_{\text{in}} - p_\pi^z - p_\gamma^z}\right] .$$

The superscripts x and z refer to the components of momentum in the x and z directions. A 3.5σ cut in $\Delta\alpha_p$ is made:

$$|\, \Delta\alpha_p \,| \leq 6.0^\circ \ . \tag{5}$$

In Fig. 8 is shown $\Delta\alpha_p$ for the raw data set, and after cuts 1–4 have been applied.

After cuts 1–5 have been made, 5.6% of the raw data set remain. This data set is referred to as the real data set. In order to more clearly see the bremsstrahlung signal we have defined a quantity m_t, the reconstructed target mass:

$$m_t = [(E_{\text{in}} - E_\pi - E_p - E_\gamma)^2 - |\, \mathbf{p}_{\text{in}} - \mathbf{p}_\pi - \mathbf{p}_p - \mathbf{p}_\gamma \,|^2]^{1/2} \ .$$

For $\pi p \to \pi p \gamma$ events, this quantity is equal to the proton mass. In Fig. 9, the difference $m_t - m_p$ is plotted for the raw data set, and all events which survive cuts 1–5. The clear peak at zero contains the $\pi^+ p \to \pi^+ p \gamma$ events. However, Figs. 8 and 9 also show that there is still back-

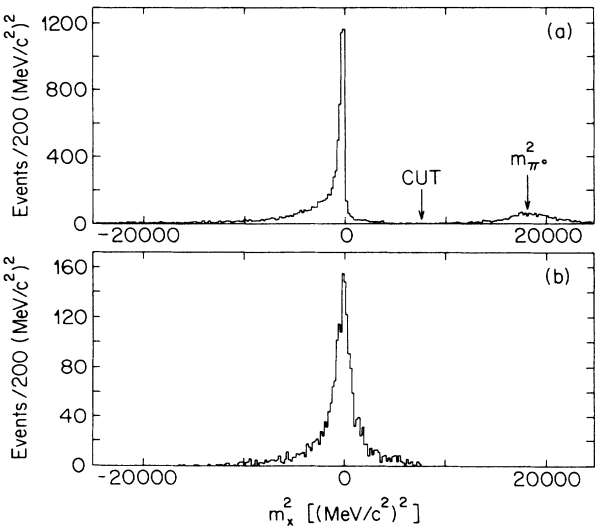

FIG. 7. Missing mass m_X^2 calculated from the initial and final pions and protons. (a) Raw data set; (b) cuts (1–4) applied. The arrow in (a) indicates cut 4.

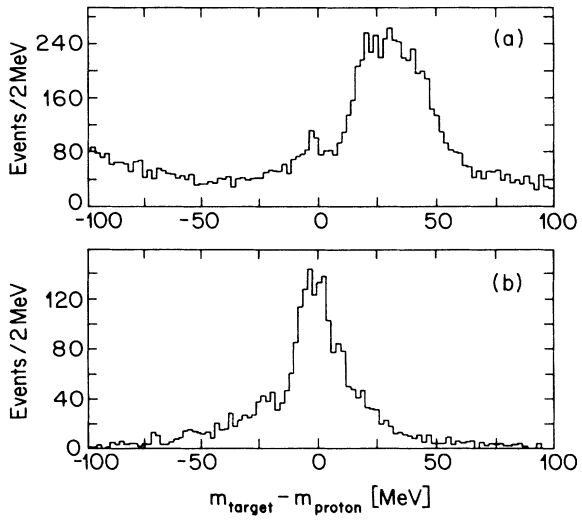

FIG. 9. Reconstructed target mass (proton mass subtracted). This quantity should be peaked at 0 for bremsstrahlung events. (a) All reconstructed events. (b) Events after cuts 1–4.

ground remaining.

Monte Carlo studies of various possible backgrounds indicate that this tail arises from nearly elastic events in coincidence with a random NaI trigger. In particular, elastic events in which the pion has decayed in the magnet. In Sec. III B it has been pointed out that by analyzing $\pi p \rightarrow \pi p \gamma$ events in which the photon comes from a later beam burst allows one to obtain a subtraction for this background. As such, the same analysis as above has been performed on a data set in which the photon came from a 6.1-ns-wide window centered about the beam burst after the πp triggering burst. These data are referred to as the background data set.

The last step in the analysis involves performing a three-constraint (3C) kinematic fit to the hypothesis that the event comes from $\pi p \rightarrow \pi p \gamma$, and cutting in the resulting χ^2-like variable. The kinematic fit includes all of the measured resolutions and then minimizes the energy and momentum balance of the $\pi p \gamma$ system. In Fig. 10, the resulting χ^2 for both the real data and the background data in three ranges of photon energies ($E_\gamma < 40$ MeV, 40 MeV $< E_\gamma < 80$ MeV, and $E_\gamma > 80$ MeV) are shown. Almost all of the background is in the lowest range of photon energies. The χ^2 is cut at 4.0, 5.5, and 7.0 in the three sets, respectively. These cuts are made where the χ^2 is flat, and results in an error of less than 1%. The nonuniformity of this cut is due to the non-Gaussian nature of the photon resolution. This cut removes 13% of the real events and 37% of the background events, which reduces the errors associated with the background subtraction. Most of the events rejected by the kinematic fitting had a fit photon energy below 20 MeV. Finally, a summary of the number of events remaining after each of the levels of analysis is given in Table I.

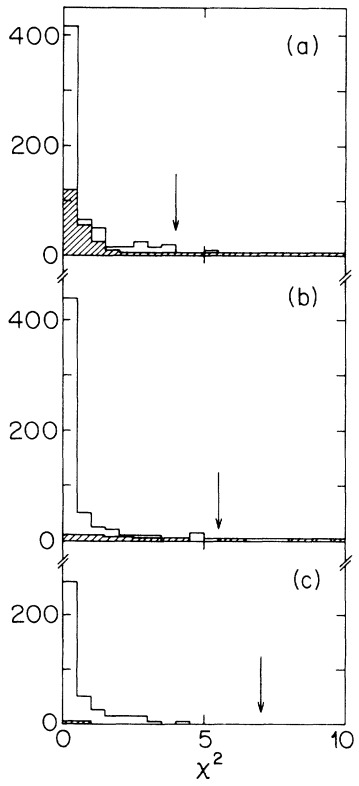

FIG. 10. χ^2 distribution after kinematic fit for both the real data and the background data (shaded histogram). (a) $E_\gamma \leq 40$ MeV. (b) 40 MeV $< E_\gamma < 80$ MeV. (c) $E_\gamma \geq 80$ MeV. The arrows indicate cuts.

D. Cross-section calculations

The cross section is calculated as

$$\frac{d^5\sigma}{d\Omega_\pi d\Omega_\gamma dE_\gamma} = \frac{N_{\text{scat}}}{N_{\text{in}}\epsilon_{\text{ch}}} \frac{1}{\Omega_\pi} \frac{1}{\Omega_\gamma} \frac{1}{\Delta E_\gamma} \frac{1}{N_{\text{proton}}} \times \frac{1}{\epsilon_\pi} \frac{1}{\epsilon_p} \frac{1}{\epsilon_\gamma} \frac{1}{\eta_{\text{decay}}} \frac{1}{\epsilon_l(E_\gamma)} .$$

N_{scat} is the number of events which survive all cuts minus the number of background events which survive the same cuts. $N_{\text{in}}\epsilon_{\text{ch}}$ is the number of incident pions corrected run by run for the chamber efficiency. N_{proton} is the number of protons per cross-sectional area in the target. Ω_π is the effective solid angle of the pion spectrometer (Fig. 3). Ω_γ is the effective solid angle of the NaI array; it does not include any energy-dependent efficiencies. ΔE_γ is the bin width in photon energy at the point evaluated; the cross section is plotted at the center of the bin. ϵ_π is the efficiency of the pion spectrometer; it includes scintillator and track-reconstruction efficiency. ϵ_p is the proton-detector efficiency and includes the detector efficiency and pile-up corrections. ϵ_γ is the efficiency of the NaI array and includes both detection and energy-dependent efficiencies. η_{decay} is the correction for pions decaying in the spectrometer, and finally ϵ_l is a correction for events lost during cuts 1–5. The values of all these quantities are given in Table II.

Table III contains measured cross sections as a function of photon energy for the entire set in 10-MeV-wide bins. This is about the energy resolution of the highest-energy photons. Because of the large angular range accepted by the pion spectrometer (55°–95°), we also split the data into a low-pion-angle ($55° < \theta_\pi < 75°$) and a high-pion-angle set ($75° < \theta_\pi < 95°$) (these angles are measured

TABLE I. A summary of the number of events in both the real data set and the background (off-time photon) data set which survive each level of cutting. Reconstruct πp means that an in-time pion and proton have been completely reconstructed. $\pi p + \gamma$ includes an in-time photon. Cuts 1,2,3 remove elastic events. Cut 4 removes events from π^0 production. Cut 5 removes quasielastic + random NaI trigger events.

Data cut	Number of surviving events: Data set	Background set
On tape	1 240 000	1 240 000
Reconstruct πp	129 900	129 900
$\pi p + \gamma$	27 072	20 740
Cuts 1,2,3 (elas. dev.)	4660	1560
Cut 4 (m_X^2)	2332	1560
Cut 5 ($\Delta\alpha_p$)	1589	410
Kinematic fitting	1376	257

TABLE II. The quantities which go into the calculation of the cross section. The quantities on which each depend are shown in parentheses. When a value varies, its range is given.

Quantity	Value
N_{in}	$(1.787\pm0.077)\times10^{12}$
N_{scat}	$(1376\pm37)-(257\pm16)$
N_p	$(613\pm3.7)\times10^{-12}$/nb
Ω_π	125 msr
Ω_γ	130 msr
ΔE_γ	10 or 15 MeV
ϵ_π	(0.86 ± 0.02)
ϵ_{ch}(time)	$(0.298\pm0.005)-(0.546\pm0.008)$
$\epsilon_p(E_p)$	$(0.77\pm0.02)-(0.86\pm0.02)$
$\epsilon_\gamma(E_\gamma)$	$(0.74\pm0.04)-(0.92\pm0.05)$
$\eta_{\text{decay}}(p_\pi)$	$(0.85\pm0.01)-(0.90\pm0.01)$
$\epsilon_l(E_\gamma)$	0.95–1.00

in the laboratory frame). In Table IV are the cross sections as measured for the entire, the low-angle and the high-angle data sets. These data are presented in 15-MeV-wide bins in photon energy to maintain the same statistical accuracy in the subsets as in the entire set in 10-MeV bins. In Figs. 11 and 12, the data in Tables III and IV are plotted.

E. Analysis of elastic data

During the run, one tape of $\pi p\to\pi p$ triggers (30 min) for every five tapes of $\pi p\to\pi p\gamma$ triggers (10 h) has been taken. The elastic data have been taken mainly for calibration of the proton detector. However, we have also analyzed some of this data to check our understanding of the pion and proton detectors. The results of the elastic data have been plotted in Fig. 13. The solid curve shows the Karlsruhe-Helsinki phase-shift results[28,29] for $p_\pi=415.8$ MeV/c. These phase shifts fit the π^+p scattering data at 408 and 427 MeV/c quite well.[30] The agreement between our data and the phase shifts is also quite good, with the χ^2/N_{DF} of the data fit to the line of 10.99/16.

We have also used the elastic cross section as a monitor of changes in the detectors, target, and pion beam. This is done for every $\pi p\to\pi p\gamma$ run by examining all events in a photon time window which did not include in-time photons. These photons are not correlated with the π and p, and provide a good sample trigger for elastic events. The resulting cross sections are then fit to the Karlsruhe-Helsinki phase shifts with one free parameter. The value of this parameter is the same for all analyzed runs, and has not been used to normalize the data.[31]

TABLE III. The measured cross section for all data, $55°\le\theta_\pi\le95°$. The photon-energy bin width is 10 MeV. All variables are in the laboratory frame.

E_γ (MeV)	$\frac{d^5\sigma}{d\Omega_\pi d\Omega_p dE_\gamma}\left[\frac{\text{nb}}{\text{sr}^2\text{MeV}}\right]$
20–30	1.63±0.27
30–40	1.23±0.23
40–50	1.37±0.20
50–60	1.45±0.18
60–70	1.29±0.16
70–80	1.19±0.15
80–90	1.11±0.15
90–100	1.02±0.14
100–110	0.80±0.13
110–120	0.67±0.10
120–130	0.61±0.11

TABLE IV. The measured cross section in 15-MeV-wide photon-energy bins. The entire data set and the two subsets in pion angle are given. θ_π is measured in the laboratory.

	$\frac{d^5\sigma}{d\Omega_\pi d\Omega_p dE_\gamma}\left[\frac{\text{nb}}{\text{sr}^2\text{MeV}}\right]$		
E_γ (MeV)	$55°<\theta_\pi<95°$	$55°<\theta_\pi<75°$	$75°<\theta_\pi<95°$
20–35	1.57±0.23	1.23±0.28	1.91±0.30
35–50	1.24±0.18	1.31±0.21	1.17±0.24
50–65	1.40±0.16	1.40±0.18	1.40±0.20
65–80	1.21±0.14	1.20±0.16	1.22±0.18
80–95	1.12±0.13	1.27±0.17	0.90±0.16
95–110	0.85±0.10	0.83±0.13	0.90±0.13
110–125	0.71±0.09	0.82±0.11	

F. Comparison to previous data

The angular acceptance of this experiment and the UCLA experiment[3] are not the same. The UCLA experiment has detected pions at 52.5° in the laboratory and photons from 180° to 260° while our pions are detected between 55° and 95° and photons are at 241°. In comparing to the UCLA data, only their data in which the photon angles are the same as ours have been examined[3] (UCLA G_7).

Figure 14 shows our low-angle data set and the UCLA G_7 data. Both sets agree within a factor of 2; exact agreement is not expected as most theories predict that the cross section rises as one goes to larger pion angles. This effect is seen in the comparison. It is also noted that a

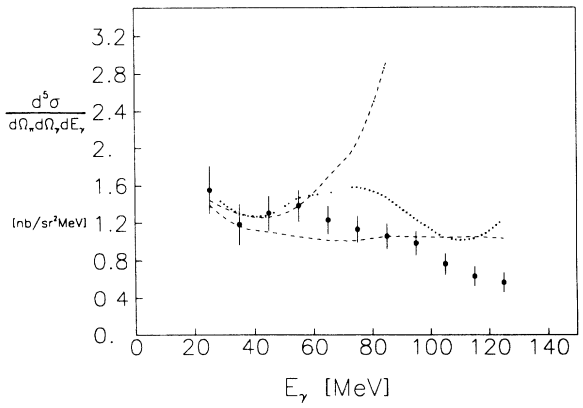

FIG. 11. The laboratory-frame $\pi^+p\to\pi^+p\gamma$ differential cross-section averaged over all pion angles, $55°\le\theta_\pi\le95°$. The three curves are theoretical predictions from SPA [—·—·—·], EED [— — —], and MIT ($\mu_\Delta=2.8\mu_p$) [· · · ·].

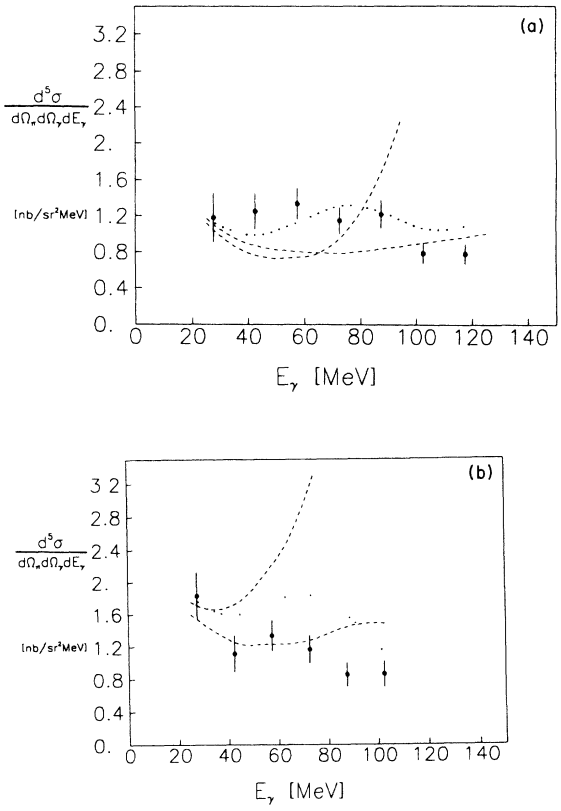

FIG. 12. The laboratory-frame $\pi^+p\to\pi^+p\gamma$ differential cross section compared to theoretical predictions. The notation is the same as in Fig. 11. (a) $55°\le\theta_\pi\le75°$. (b) $75°\le\theta_\pi\le95°$.

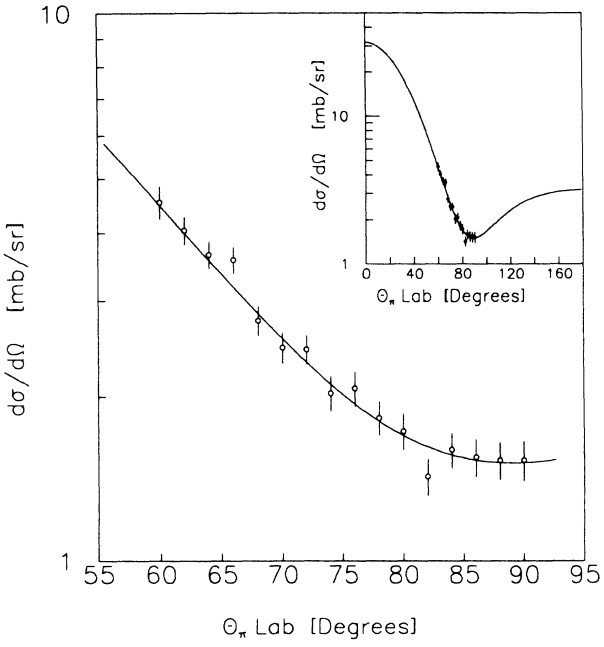

FIG. 13. Measured laboratory-frame elastic cross section compared to the cross section reconstructed from the Karlsruhe-Helsinki phase shifts at $p_\pi=415.8$ MeV/c.

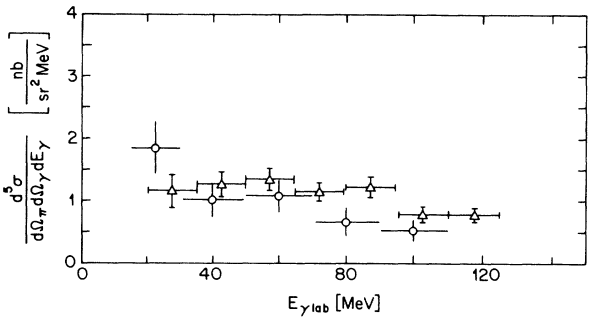

FIG. 14. A comparison of the data in low-angle data set [Δ]($55°\le\theta_\pi\le75°$), to the UCLA G_7 data [○] ($\theta_\pi=52.5°$, $\theta_\gamma=240°$).

slight bump at intermediate energies hinted at in the UCLA data is seen at about the same level in our data.

It is not possible to further reduce the range of pion angles without seriously affecting the statistics of the data set. In this regard we are unable to form a data sample that more closely matches the UCLA geometry. The two data sets remain essentially complementary. The UCLA data mapping out the cross section as a function of photon angle at a fixed pion angle, and this data holding the photon angle fixed and varying the pion angle.

IV. COMPARISON TO THEORETICAL CALCULATIONS

A. The SPA theory

In Figs. 11 and 12, the SPA calculations are compared to this data [the SPA calculation is of the four diagrams shown in Figs. 1(a)–1(d)]. SPA gives a good fit to the entire data set for photon energies below 40 MeV. In the low-angle set the cross section is underestimated, although the shape is correct up to about 60 MeV. For the high-angle set, SPA agrees at the lowest data point and then turns sharply up. Our results are in agreement with the UCLA results that SPA is valid for photon energies below 40 MeV. We have not compared our data with the predictions of Liou and Nutt[7] because of the complexity in carrying out their SPA calculation.

B. The EED model

In fitting to EED (external emission dominance)[6] we have encountered some problems for high-photon energy and large pion angles. The EED cross section starts to rise, which is not expected from the model with its supposed $1/E_\gamma$ falloff. This problem has been treated in the Appendix. All fits are made with the Mandelstam variables s and t chosen to be their average over initial and final states.[6]

Comparisons to EED are shown in Figs. 11 and 12. In fitting the low-angle set, EED underestimates the cross sections at intermediate energies; however it is quite good at both high and low photon energies. The poor fit at middle energies may be indicative of internal structure (which is not included in EED) or of off-mass-shell effects. In the high-angle set, there is good agreement out to about 70 MeV after which EED starts to rise. For this

data, EED fits the data much better than the MIT theory (next section).

C. The MIT theory

To interpret this data in terms of electromagnetic moments of the Δ^{++}, a good theoretical understanding of the process $\pi p \to \pi p \gamma$ is required. It is not at all obvious how a bremsstrahlung cross section $d^5\sigma/d\Omega_\pi d\Omega_p dE_\gamma$ is related to the magnetic dipole moment of the Δ. A good theory relating the two would include (1) as many partial waves in the πp scattering as possible, (2) a correct treatment of the off-mass-shell πp amplitudes, and (3) the correct gauge-fixing terms for the calculated amplitude. The MIT theory is a dynamically consistent, gauge-invariant model for πN bremsstrahlung involving an isobar model which is fitted to experimental phase shifts. The model includes $P33$, $S31$, and $P31$ partial waves.[17]

For each included partial wave, the $\pi N\Delta$ vertex is parametrized as

$$\frac{f_{\pi N\Delta}}{m_\pi} h(q^2) = \frac{g}{\alpha^2 + q^2} ,$$

giving two free parameters g and α for each partial wave. There is also a mass parameter, m_Δ, in the spin-$\frac{3}{2}$ propagator G_Δ:

$$G_\Delta = (E - m_\Delta - \Sigma_\Delta)^{-1} ,$$

where Σ_Δ is a self-energy correction. The free parameters are obtained by fitting to the experimental πN phase shifts for each partial wave (Table V). For the P33 wave two different sets of the parametrizations result, both giving good fits to the data. The first set is slightly better, and is used in the bremsstrahlung calculation.[17] When bremsstrahlung is calculated in this model, the electromagnetic moments of the Δ enter as parameters. It has been shown that the effect of the quadrupole moment is beyond the sensitivity of an experiment of our type.[16] The only moment to which one is sensitive is μ_Δ, the magnetic dipole moment. When the MIT theory is fitted to the UCLA data,[17] $2.5\mu_p \le \mu_\Delta \le 3.5\mu_p$ is obtained.

TABLE V. The free parameters in the MIT theory. There are two different parametrizations for the P33 wave.

Partial wave	$\alpha(\text{fm}^{-1})$	g	m_Δ (MeV)
P33	$\alpha = 1.2$	$g = 2.12/(m_\pi)^{3/2}$	1445
P33	$\alpha = 2.2$	$g = 1.79/(m_\pi)^{3/2}$	1322
S31	$\alpha_s = 5.75$	$g_2 = 0.36/m_\pi$	
P31	$\alpha_p = 2.09$	$g_p = 2.74/m_\pi^2$	

When comparing with the MIT theory, there are uncertainties in the off-mass-shell treatment and ambiguities in the parametrization of the $\pi N\Delta$ vertex which make it impossible to obtain μ_Δ to an accuracy better than $\pm .25\mu_p$ (Ref. 16) from an unpolarized measurement such as this one. Also, the model is valid only for $E_\gamma < \Gamma_\Delta$ (116 MeV) and when compared to our data, $E_\gamma = 100$ MeV might be a more realistic limit.

In fitting, a program provided by a member of the MIT group[32] has been used to average the theory over the detector acceptance for several values of μ_Δ. We have also done point calculations in which we assumed all events came from the center of the target, and all particles were centered in their detector. The results of the folding and of the point calculations are given in Table VI. With the averaged theory values, a χ^2/N_{DF} for each value of μ_Δ is then calculated:

$$\chi^2/N_{\text{DF}} = \frac{1}{n-1} \sum_{i=1}^{n} \left[\frac{d^5\sigma^{\text{meas}}/d\Omega_\pi d\Omega_\gamma dE_\gamma(E_\gamma)_i - d^5\sigma^{\text{MIT}}/d\Omega_\pi d\Omega_\gamma dE_\gamma(E_\gamma,\mu_\Delta)_i}{\sigma_i(E_\gamma)} \right]^2 ,$$

TABLE VI. The MIT theory averaged over the detector acceptance, and point calculations at several values of μ_Δ. The low-angle point calculations are at $\theta_\pi = 67°$, $\theta_\gamma = 241°$. The high-angle point calculations are at $\theta_\pi = 83°$, $\theta_\gamma = 241°$.

	$55° \le \theta_\pi \le 75°$						$75° \le \theta_\pi \le 95°$					
E_γ	$\mu_\Delta = 2.0\mu_p$		$\mu_\Delta = 2.5\mu_p$		$\mu_\Delta = 3.0\mu_p$		$\mu_\Delta = 2.0\mu_p$		$\mu_\Delta = 2.5\mu_p$		$\mu_\Delta = 3.0\mu_p$	
(MeV)	Pt.	Avg.	Pt.	Avg.	Pt.	Avg.	Pt.	Avg.	Pt.	Avg.	Pt.	Avg.
27.5	1.04	1.10	1.05	1.11	1.07	1.13	1.54	1.71	1.58	1.74	1.62	1.78
42.5	0.81	0.87	0.87	0.93	0.97	1.03	1.38	1.45	1.46	1.53	1.57	1.63
57.5	0.79	0.87	0.95	0.99	1.20	1.24	1.47	1.52	1.60	1.65	1.82	1.87
72.5	1.00	1.01	1.11	1.12	1.49	1.50	1.61	1.58	1.71	1.69	1.99	1.99
87.5	1.32	1.36	1.17	1.17	1.42	1.39	1.66	1.64	1.54	1.52	1.71	1.69
102.5	1.74	1.81	1.19	1.21	1.05	1.05	1.65	1.67	1.26	1.23	1.17	1.13
117.5	2.12	2.31	1.34	1.44	0.89	0.92	1.63	1.76	1.13	1.17	0.85	0.85

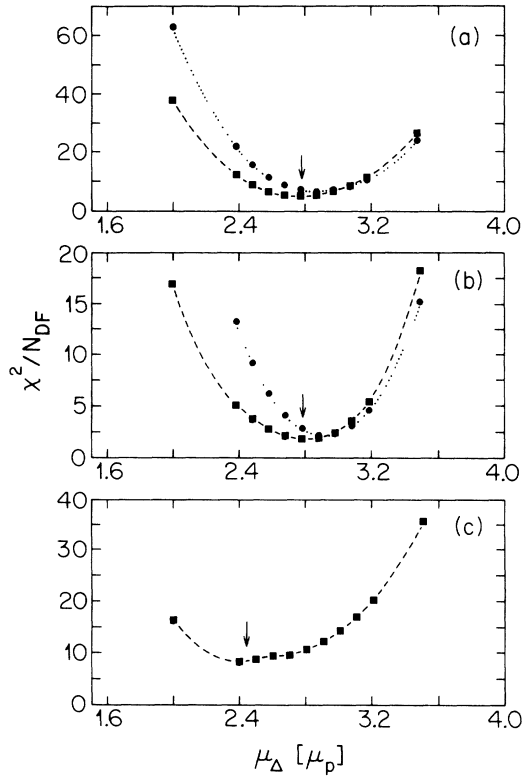

FIG. 15. χ^2 per degree of freedom for the fits of the MIT theory to the data. All data: ●; data with $E_\gamma \leq \Gamma_\Delta$: ■. (a) Entire data set; (b) low-angle data set; (c) high-angle data set. The arrows indicate the minimums of the restricted (■) data.

where $\sigma_i(E_\gamma)$ is the 1σ error of each measured point, $d^5\sigma^{\text{meas}}$ is the measured cross section, and $d^5\sigma^{\text{MIT}}$ is the averaged MIT cross section. The results both including and excluding points with $E_\gamma > \Gamma_\Delta$ are shown in Fig. 15. The fits obtained for the entire data set and those for the high-angle data set are not particularly good. The minimum of χ^2/N_{DF} being greater than 4 in both cases. For the low-angle set, a minimum at $\mu_\Delta = 2.80\mu_p$ with a χ^2/N_{DF} of just under 2 is obtained. From only the low-angle data, we obtain

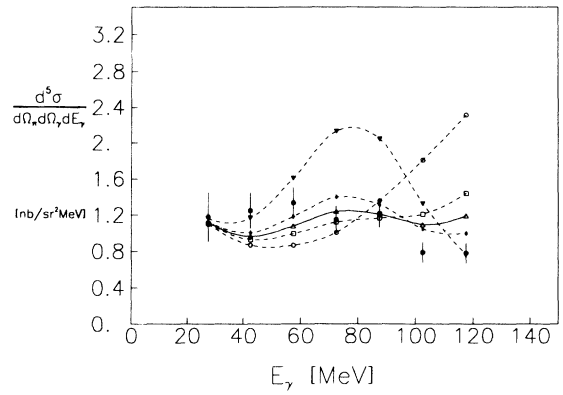

FIG. 17. MIT theory at several values of μ_Δ compared to the low-angle data set ($55° \leq \theta_\pi \leq 75°$). The notation is the same as in Fig. 16.

$$2.55\mu_p < \mu_\Delta < 3.05\mu_p \ ,$$

and, when combined with the theoretical uncertainty,

$$2.30\mu_p < \mu_\Delta < 3.30\mu_p \ .$$

The errors have been added linearly because of the nature of the theoretical errors; the ambiguities in the choice of the vertex form factors causes a shift in the theory, and cannot be treated as a random error. Finally, a fit to only the data with $E_\gamma < 100$ MeV still gives a poor fit to the high-angle data set, but a slightly better fit to the low-angle set, and nearly the same value of μ_Δ. Figures 16, 17, and 18 show the MIT theory at several values of μ_Δ plotted against this data.

In examining the fits to the UCLA data,[14,17] we observe that the MIT theory gives the best fits to the UCLA data when the photon is out of plane by 36° (in the angles defined in the UCLA experiment, $\tan\alpha = \tan\theta\cos\phi$ and $\sin\beta = \sin\theta\sin\phi$, this is at $\beta_\gamma = 36°$). The fits to the UCLA data at $\beta_\gamma = 0°$ appear no better, and perhaps worse than the fits to our data. Also as the angle between the pion and photon became smaller, $\alpha_{\pi\gamma}$, the MIT theory begins to overestimate the UCLA data ($\alpha_\gamma = 160°$). This is the same effect observed in our high-angle data set. In the

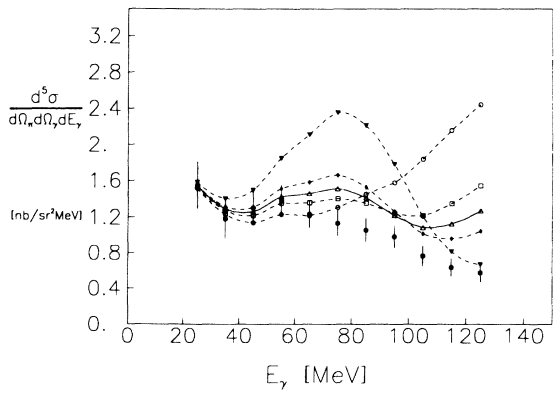

FIG. 16. MIT theory at several values of μ_Δ compared to the entire data set ($55° \leq \theta_\pi \leq 95°$). ○: $\mu_\Delta = 2.0\mu_p$, □: $\mu_\Delta = 2.5\mu_p$, △: $\mu_\Delta = 2.7\mu_p$, ◇: $\mu_\Delta = 2.9\mu_p$, ▼: $\mu_\Delta = 3.5\mu_p$, ●: data.

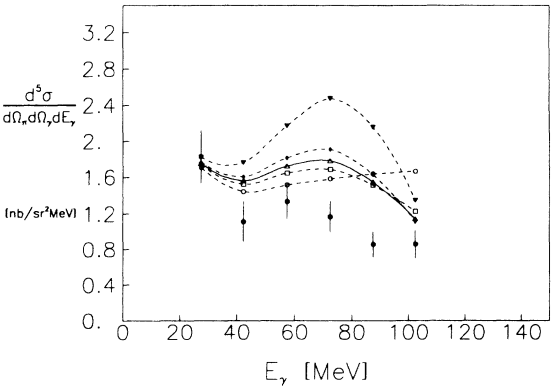

FIG. 18. MIT theory at several values of μ_Δ compared to the high-angle data set ($75° \leq \theta_\pi \leq 95°$). The notation is the same as in Fig. 16.

center-of-mass frame, our high-angle data set, and the UCLA data at $\alpha_\gamma = 160°$, $\beta_\gamma = 0°$ have nearly the same E_γ, p_π, and $\alpha_{\pi\gamma}$. The fact that the theoretical cross sections are too high for both data sets may imply that there is some off-mass-shell effect which needs to be examined.

In the geometries for all $\pi p\gamma$ experiments to date, the detectors are located near the point of maximum destructive interference for external radiation, thus maximizing the contribution of any internal radiation. It is near this point where the MIT fits the data quite well. However, at the most extreme deviations from this optimum geometry the theory has tended to overpredict the measured cross sections, while a much simpler prescription such as EED has continued to fit the data reasonably well.

V. CONCLUSIONS

We have measured the cross section $d^5\sigma/d\Omega_\pi d\Omega_p dE_\gamma$ from the process $\pi^+ p \to \pi^+ p\gamma$ as pion incident energies of 299 MeV. The photon is detected at 119° from the incident beam, while the pion is detected between $\theta_\pi = 55°$ and $\theta_\pi = 95°$ on the opposite side of the incident pion beam in a coplanar geometry. In comparing this data to SPA calculations, we find agreement for photon energies up to 40 MeV. We find that EED underestimates the cross section in our low-angle data set, but does fairly well in the high-angle data set up to photon energies of about 70 MeV. The fact that the EED cross sections are low in the low-angle data may indicate some underlying structure in the data.

Finally, we fit our data with the MIT theory in order to obtain a measurement of μ_Δ. We find that the MIT theory does a reasonable job of fitting our low-angle data, but overestimates our high-angle data above 50 MeV by about 50%. In measuring μ_Δ, it is not possible to make use of the high-angle data set because of the poor fit of all the curves. We are forced to extract a value of μ_Δ exclusively from the low-angle data set. From this set alone we get that $\mu_\Delta = (2.80 \pm 0.25)\mu_p$. To this we have to add the theoretical uncertainty of $\pm 0.25\mu_p$. This gives us $\mu_\Delta = (2.8 \pm 0.5)\mu_p$ and is consistent with the result quoted by the MIT group from their fits to the UCLA data,[17] $\mu_\Delta = (3.0 \pm 0.5)\mu_p$. However, these values of μ_Δ are entirely dependent upon the validity of the MIT theory.

ACKNOWLEDGMENTS

We would like to thank the staff and crews of SIN for their assistance and hospitality during our runs. We thank J. A. Bistirlich for his work on our hydrogen target and R. Frosch for his help with the $\pi E1$ beam. This work was supported by the Swiss Agency for Basic Research (Schweizerischer Nationalfonds), the Director, Office of Energy Research, Division of Nuclear Physics of the Office of High Energy and Nuclear Physics of the U.S. Department of Energy under Contract DE-AT03-81ER4000, and the National Science Foundation under Grant PHY-8519381.

APPENDIX

The EED (external emission dominance) model has been developed to fit the UCLA experimental data when other models at the time have been unable to do so.[6] This prescription has no theoretical footing, it just gives very good fits to the UCLA data. EED is essentially only the $1/k$ term in the SPA theory. When we try to fit EED to our data, we discover what at first appears to be a very strange behavior in EED. For high photon energies and large pion angles, the EED cross section begins to rise with photon energy. A behavior quite at odds with the expected $1/k$ falloff. In this appendix we explain the source of this effect.

The EED model gives the bremsstrahlung cross section as

$$\frac{d^5\sigma}{d\Omega_\pi d\Omega_\gamma dE_\gamma} = -e^2 A^\mu A_\mu \left[\frac{d\sigma}{d\Omega}(s,t)\right]_{\pi p} \Phi ,$$

where

$$A^\mu = -\frac{q_1^\mu}{q_1\cdot k} - \frac{p_1^\mu}{p_1\cdot k} + \frac{q_2^\mu}{q_2\cdot k} + \frac{p_2^\mu}{p_2\cdot k}$$

and Φ is a phase-space factor given as

$$\Phi = \frac{1}{2(2\pi)^3}\frac{\sqrt{s}}{q_1}\frac{q_2^3 k}{q_2^2(\sqrt{s}-k) + E'_\pi(q_2\cdot k)} .$$

q_1 and q_2 are the incident and final pion momentums, p_1 and p_2 are the incident and final proton momentums, k is

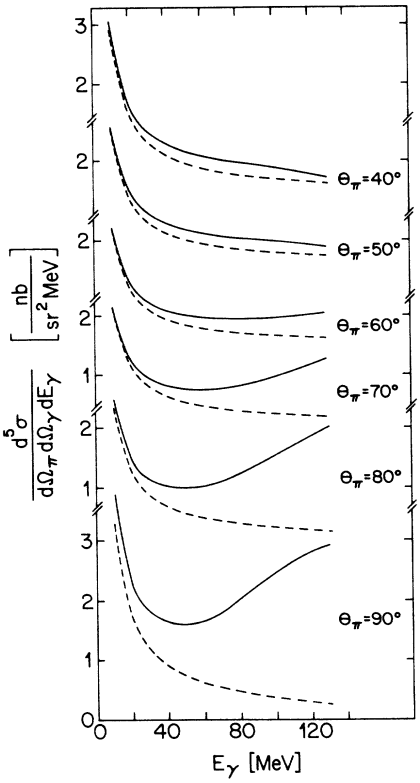

FIG. 19. The EED predictions for two choices of s and t at several pion angles. The solid curves are EED (s_1,t_1), and the dashed lines are EED (s_2,t_2). s_1 and t_1 are defined as the average between initial- and final-state values of these variables, while s_2 and t_2 are the initial s and the elastic value of t. The vertical scale is linear, and the same for each section of the plot.

the photon energy, E'_π is the final pion's energy, and s and t are the usual Mandelstam variables. There are two choices of s and t which can be used for bounding the EED predictions:[6]

$$s_1=\bar{s}=\tfrac{1}{2}[(q_1+p_1)^2+(q_2+p_2)^2] ,$$

$$t_1=\bar{t}=\tfrac{1}{2}[(q_1-q_2)^2+(p_1-p_2)^2] ,$$

and

$$s_2=s_{\text{in}}=(q_1+p_1)^2 ,$$

$$t_2=t_{\text{elastic}}=2\,|\,\mathbf{q}_1\,|^2(1+\cos\theta_\pi) ,$$

where θ_π is in the center-of-mass frame. When fits are made to the UCLA data ($\theta_\pi^{\text{lab}}=52°$) both choices of s and t give essentially the same cross sections. However as one moves to pion angles larger than 50° this is no longer true. In Fig. 19 we plot the EED predictions for both choices of s and t at various pion angles.

The rising cross section can be understood if we examine the individual contributions to the EED prediction. The $A_\mu A^\mu\Phi$ term is only weakly dependent upon the choice of s and t and gives essentially a $1/k$ falloff. However the $d\sigma/d\Omega(s,t)$ can vary substantially. For the energies of interest in this calculation we are above the $\Delta(1232)$ resonance. This means that as s decreases from s_2 to s_1, the total πp cross section is increasing. However, as t goes from t_2 to t_1, we are moving to more backward pion angles. For forward pion angles, the fall in cross section as we move to backward angles just cancels the rise caused by s, and gives us that $d\sigma/d\Omega$ is approximately constant. However, at large enough pion angles the cross section stops falling and begins to rise. This means that the contributions from s and t are both varying in the same direction, and cause the EED cross section to rise.

For the s_2,t_2 case, the resulting cross sections are seen to fall with at least the expected shape. However, the difference between the two choices becomes quite large at the largest pion angles, and our data at these angles falls between the two curves. In the case of the UCLA data, θ_π was 52°, where the difference between the two choices was never very large (under 15%) and the fits were quite good. While in our data, the place where EED fits worst is exactly where the large differences begin to occur. In order to be able to make predictions with EED, it is necessary that the differences between the two choices of s and t be small relative to the cross section itself.

---

*Current address: Physik-Institut der Universität Zürich, CH-8001 Zürich, Switzerland.

†Current address: Clinique del'Université, Bruxelles, Belgium.

‡Current address: Physikalisches Institut der Universität Heidelberg, D-6900 Heidelberg, Germany.

§Current address: Stanford Linear Accelerator Center, Stanford, California 94305.

[1]D. I. Sober, M. Arman, D. J. Blasberg, R. P. Haddock, K. C. Leung, B. M. K. Nefkens, B. L. Schrock, and J. M. Sperinde, Phys. Rev. D **11**, 1017 (1975).

[2]K. C. Leung, M. Arman, H. C. Ballagh, Jr., P. F. Glodis, R. P. Haddock, B. M. K. Nefkens, and D. I. Sober, Phys. Rev. D **14**, 698 (1976).

[3]B. M. K. Nefkens, M. Arman, H. C. Ballagh, P. F. Glodis, R. P. Haddock, K. C. Leung, D. E. A. Smith, and D. I. Sober, Phys. Rev. D **18**, 3911 (1978).

[4]S. Playfer *et al.*, J. Phys. G **13**, 297 (1987).

[5]F. E. Low, Phys. Rev. **110**, 974 (1958).

[6]B. M. Nefkens and D. I. Sober, Phys. Rev. D **9**, 2434 (1976).

[7]M. K. Liou and W. T. Nutt, Phys. Rev. D **16**, 2176 (1977).

[8]W. E. Fischer and P. Minkowski, Nucl. Phys. **B36**, 519 (1972).

[9]L. A. Kondratyuk and L. A. Ponomarev, Yad. Fiz. **7**, 111 (1967) [Sov. J. Nucl. Phys. **7**, 82 (1968)].

[10]V. I. Zakharov, L. A. Kondratyuk, and L. A. Ponomarev, Yad. Fiz. **8**, 783 (1968) [Sov. J. Nucl. Phys. **8**, 456 (1969)].

[11]R. Baier, L. Pittner, and P. Urban, Nucl. Phys. **B27**, 589 (1971).

[12]D. S. Beder, Nucl. Phys. **B84**, 362 (1975).

[13]P. Pascual and R. Tarrach, Nucl. Phys. **B134**, 133 (1978).

[14]Jose C. Martinez, Ph.D. thesis, MIT (1981).

[15]E. J. Moniz, Nucl. Phys. **A374**, 557c (1982).

[16]Shunzo Kumano, Ph.D. thesis, MIT (1985).

[17]L. Heller, S. Kumano, J. C. Martinez, and E. J. Moniz, Phys. Rev. C **35**, 718 (1987).

[18]S. Coleman and S. L. Glashow, Phys. Rev. Lett. **6**, 423 (1961).

[19]M. A. Bëg, B. W. Lee, and A. Pais, Phys. Rev. Lett. **13**, 514 (1964).

[20]G. E. Brown, M. Rho, and V. Vento, Phys. Lett. **97B**, 423 (1980).

[21]*SIN Users Handbook* (SIN, Villigen, Switzerland, 1981), p. 87.

[22]J. C. Alder *et al.*, Nucl. Instrum. Methods **160**, 93 (1979).

[23]G. S. Kyle *et al.*, Phys. Rev. Lett. **52**, 974 (1984).

[24]R. Stamminger, Ph.D. thesis, University of Erlangen (1983).

[25]A. Bay, Ph.D. thesis, Université de Lausanne (1986); A. Bay *et al.*, Phys. Lett. **134B**, 445 (1986); A. Bay *et al.*, Nucl. Instrum. Methods (to be published).

[26]J. Bystricki and F. Lehar, Physik-Daten **11**, 1 (1978).

[27]J. F. Janni, Proton Range-Energy Tables At. Data Nucl. Data Tables **27**, 147 (1982).

[28]G. Höhler *et al.*, *Handbook of Pion-Nucleon Scattering* (Karlsruhe, Germany, 1978).

[29]R. Koch and E. Pietarinen, Nucl. Phys. **A336**, 331 (1980).

[30]M. E. Sadler *et al.*, Phys. Lett. **119B**, 69 (1982).

[31]C. A. Meyer, Ph.D. thesis, University of California, Berkeley, 1987; Report No. LBL-23688, 1987 (unpublished).

[32]Shunzo Kumano, private communication.